AVIRIS Calibration and Application in Coastal Oceanic Environments: Tracers of Soluble and Particulate Constituents of the Tampa Bay Coastal Plume*

Abstract

AVIRIS is a test bed for future spacecraft sensors such as HIRIS and MODIS planned for the Earth Observing System. Model-derived absorption coefficients at 415 nm, a(415), and back-scattering coefficients at 671 nm, b_b(671) for Tampa Bay waters were used to create images from AVIRIS data of the dissolved component of a(415) due to gelbstoff, a_g(415), and salinity. Images of a_g(415), salinity, and b_b(671) were used to depict the distribution of dissolved and particulate constituents, respectively, for Tampa Bay plume during late, ebb-tidal conditions. Salinity covaried with a_g(415), which provided a means of mapping salinity from the a_g(415) imagery. The concentration of suspended particles, as inferred from b_b(671), was extremely variable in the shallow regions where waves and currents interacted. Pollutants covarying with fresh water or suspended sediments can be mapped from a_g(415) and b_b(671) images, respectively.

Introduction

The effluent from large rivers such as the Amazon and Orinoco contains pigments and colored dissolved organic matter (CDOM), or gelbstoff, that affect the spectral radiance ratios reaching ocean-color satellite or aircraft sensors. These large river plumes can be addressed using large-pixel (1-km) sensors such as the Coastal Zone Color Scanner or the planned Sea-WiFS instruments (Muller-Karger *et al.*, 1988; 1989). Higher spectral and spatial resolution are necessary when studying small estuaries (Carder *et al.*, 1992).

If the absorption, a_g, due to gelbstoff can be derived from satellite or aircraft spectral imagery, then it may be possible to convert a_g images into salinity images. For many estuaries a conservative mixing or dilution behavior (e.g., a_g linear with salinity) for the optical properties of the dissolved material permits derivation of the salinity field from the optical field (Berger et al., 1984), although for a given estuary the mixing relationship typically changes with time as a function of runoff. If a salinity-pollutant relationship is known, however, then dissolved pollutants that are transported with the low-salinity plume may be mapped.

The Airborne Visible-InfraRed Imaging Spectrometer (AVIRIS) of NASA was flown over the effluent plume of Tampa Bay. AVIRIS is a test bed for future spacecraft imaging spectrometers such as the High-Resolution Imaging Spectrometer (HIRIS) planned to orbit in 2003 as part of the Earth Observing System (EOS). AVIRIS was designed largely for high spectral and spatial resolution land applications with target reflectances of 20 to 50 percent, whereas water reflectances are typically much less than 5 percent. It has 224 spectral channels from 400 to 2400 nm, 20-metre square pixels when viewing the Earth from 65,000 feet altitude, and about 10 to 20 percent of the signal-to-noise (S/N) of the Coastal Zone color Scanner (CZCS). For its data to be consistent with the needs of oceanographers, the S/N must be increased 10 to 20 fold (Hamilton *et al.*, 1991). For coastal applications with much larger signals, an S/N increase of 5 to 10 fold may suffice, values easily obtainable with HIRIS.

The AVIRIS preflight calibration was adjusted to be consistent with the in-flight performance of the instrument, and the S/N was increased from 20 to 50 fold by pixel binning (Carder *et al.*, 1992). The recalibrated data representing total radiance at the sensor were then partitioned into atmospheric radiance and radiance upwelled from beneath the water surface (water-leaving radiance). The spectral, water-leaving radiance curves were then converted using a model into absorption and backscattering coefficients (Carder *et al.*, 1992).

Partitioning the absorption coefficient into parts due to water, particles, and gelbstoff or CDOM, then, will permit salinity maps to be developed given a salinity-versus-gelbstoff absorption relationship. The backscattering-coefficient image provides a measure of the distribution of suspended sediments, which varies dramatically in shoal areas impacted by waves and currents. Pollutants covarying with the freshwater plume or suspended bottom sediments can conceiveably be mapped, as well, given monotonic relationships with salinity or the backscattering coefficient.

Methods

AVIRIS data were collected from a NASA ER-2 aircraft flying at 65,000 feet altitude on two SW-NE flight lines. These lines

*Presented at the First Thematic Conference on Remote Sensing for Marine and Coastal Environments, New Orleans, Louisiana, 15–17 June 1992.

K. L. Carder, R. G. Steward, R. F. Chen, S. Hawes, and **Z. Lee**
Marine Science Department, University of South Florida, 140 Seventh Avenue South, St. Petersburg, FL 33701–5016.

C. O. Davis
Jet Propulsion Laboratory, 488 Oak Grove Drive, M/S 300–323, Pasadena, CA 911–8099.

Photogrammetric Engineering & Remote Sensing, Vol. 59, No. 3, March 1993, pp. 339–344.

0099-1112/93/5903–339$03.00/0

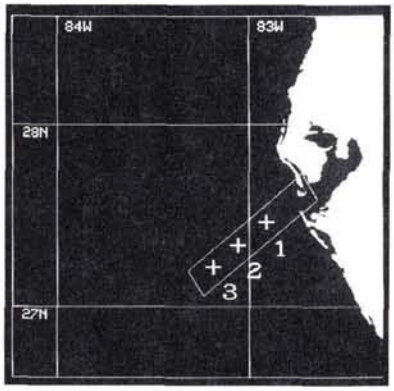

(a)

Figure 1. (a) Region covered imaged by AVIRIS scenes from two flight lines into the mouth of Tampa Bay. Also shown are three calibration stations. (b) Detailed schematic of Scene 7 of the north flight line (after Carder *et al.* (1992)).

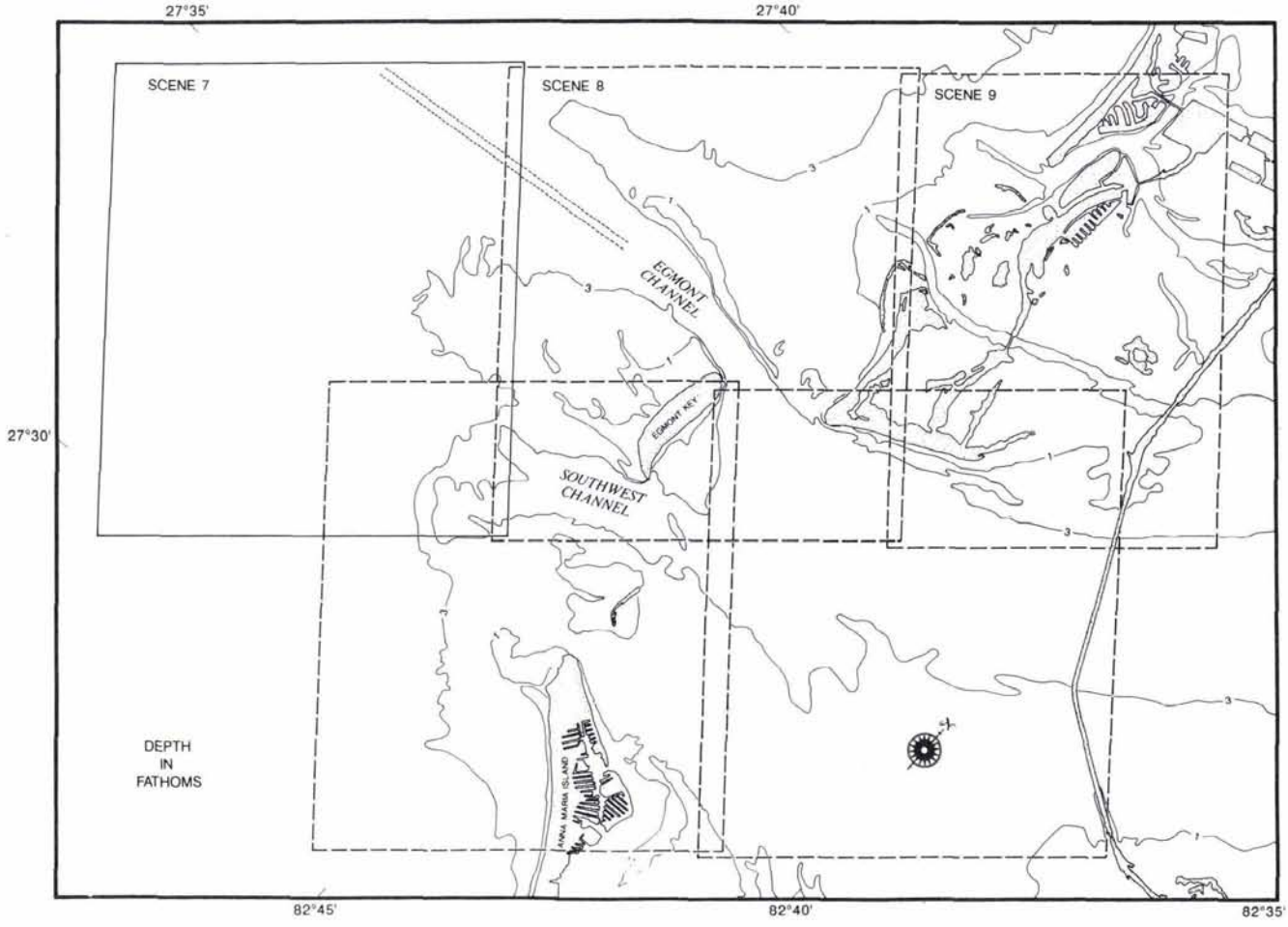

(b)

were flown at about 1515 Eastern Standard Time on 4 March 1990 and extended from the west Florida shelf over the mouth of Tampa Bay (see Figure 1). A total of 16 scenes were collected along a shelf transect covered the same day by the R/V *Bellows* of the Florida Institute of Oceanography (see Figure 1a). The shoreward scenes included complex bathymetric and topographic features (see Figure 1b) that were expected to have effects on the wave and light fields as

well as the hydrodynamics. The flights occurred during low tidal conditions when the tidal plume from Tampa Bay was fully extended offshore.

Chlorophyll *a*, pheophytin *a*, absorption coefficients, remote-sensing reflectance (R_{rs}), above-water downwelling irradiance ($E_d(0^+)$), subsurface downwelling irradiance ($E_d(z)$), and subsurface upwelling irradiance ($E_u(z)$) and radiance ($L_u(z)$) data were gathered at three stations along the transect between 0930 and 1330 hours on 4 March 1990. A second cruise on 11 May 1992, following a similar but longer offshore transect, was undertaken to gather a more extensive data set.

The pigments were determined using the fluorometric method of Holm-Hansen and Riemann (1978). The samples were collected with Niskin bottles, filtered onto 25-mm Whatman GF/F glass-fiber pads, and extracted with methanol. Salinity measurements were made by using an AGE salinometer model 2100 calibrated with Copenhagen Water for samples collected in 1992. In 1990, a Seabird[R] *in-situ* salinity sensor, integrated with the Biospherical instrument described below, was used.

Particle absorption coefficients (a_p) were determined for particles collected on Whatman GF/F glass fiber filter pads using the method of Mitchell (1990). The absorption coefficient due to colored dissolved organic matter or gelbstoff (a_g) was determined by the method of Bricaud *et al.* (1981) for material passing through preflushed, 47-mm, Nuclepore pads with 0.2-micrometre pore diameters. A Cary model 17D spectrophotometer was used to measure a_g for water-color samples in a 10-cm quartz cell.

Remote sensing reflectance and other optical measurements along with modeling results used to calibrate and validate AVIRIS radiance results have been derived in a separate contribution (Carder *et al.*, 1992). Methods for removal of atmospheric effects from AVIRIS were reported in the same article.

Results

AVIRIS-derived R_{rs} spectra were tested against field spectra in Carder *et al.* (1992) with generally favorable results, and R_{rs} model data compared very closely with AVIRIS spectra. For spectral and spatial regions where bottom reflection effects were negligible, derived images or maps of the absorption coefficient $a(415)$ and the backscattering coefficient $b_b(671)$ were derived. As this contribution concentrates on the conversion of those images to maps of salinity, the modeling activities only will be outlined here.

For an optically-thick, homogeneous ocean (e.g., well-mixed, deep water), the following equation (Morel and Prieur, 1977; Carder and Steward, 1985; Carder *et al.*, 1992) can be applied. Remote-sensing reflectance (R_{rs}) is defined as the water-leaving-radiance (L_w) fraction of the downwelling irradiance ($E_d(0^+)$) just above the sea surface, and it can be approximated by

$$R_{rs}(\lambda) = L_w(\lambda)/E_d(\lambda) = [0.33 b_b(\lambda)/\{a(\lambda) + b_b(\lambda)\}]\,(t/n)^2/Q \qquad (1)$$

where Q is $E_u(\lambda)/L_u(\lambda)$, only weakly dependent upon λ (Gordon and Morel, 1983), $b_b(\lambda)$ is the backscattering coefficient of water and its suspended particles, and the squared term provides for the radiance divergence and sea-air transmittance, t, of radiance leaving the water. The index of refraction of seawater, n, is about 1.334. This equation contains no provision for transpectral phenomena such as water-Raman scattering (considered negligible for nearshore environments) or fluorescence due to CDOM and chlorophyll *a* (not necessarily negligible for certain wavelengths). Provision for these

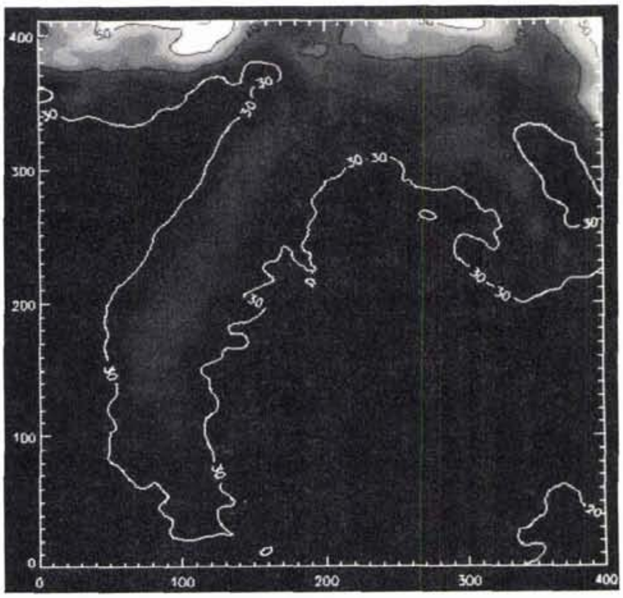

Figure 2. Horizontal variation of $b_b(671)$*1000 for Scene 7. Values have been smoothed by a 14-by-14-pixel boxcar average to increase S/N and to reduce contour complexity.

can be made by adding additional terms (e.g., see Gordon (1979), Carder and Steward (1985), Stavn (1990), and Marshall and Smith (1990)), but are typically unnecessary for short (near 400 nm) and long (>600 nm except 685 ± 7 nm) wavelengths.

For the longer wavelengths (e.g., > 600 nm) the absorption coefficient starts to be dominated by molecular absorption of water a_w. At 671 nm $a_w = 0.43\ m^{-1}$, which is much larger than the other absorption components measured at Station 1. This value was taken for the total absorption coefficient and assumed constant throughout Scene 7 (see Figure 1b) Then Equation 1 was solved for $b_b(671)$, using the Q value derived for Station 1 (Carder *et al.*, 1992).

The horizontal variation of the backscattering coefficient is illustrated in Figure 2. In this near-shore environment, the variability in the backscattering coefficient is significantly affected by suspended sediments carried by the ebb tidal currents from Tampa Bay and sediments locally resuspended from shoal areas by waves from the northwest. The tidal currents usually flow out from channels north and south of Egmont Key (Figure 1b), and the flows from these two conduits appear to converge at the bright, central shoal region in the top-central portion of the scene. The resulting sediment plume dominates the central portion of the image. Beneath this plume, water depths increase offshore to 13 m. A second shoal region is found offshore from Anna Maria Island which is influenced by waters leaving Southwest Passage (the dark region in the upper right-hand portion of the image). Here the diverging current appears to suspend and carry sediment streamers offshore as well. It is not clear from this image how much of the backscattering is due to wave-suspended, sandy sediments that will rapidly settle out of the water column, and how much is due to organic particles and fine sediments which may be transported significant distances. Comparison with a plume image dominated by a more conservative constituent such as CDOM will at least permit a

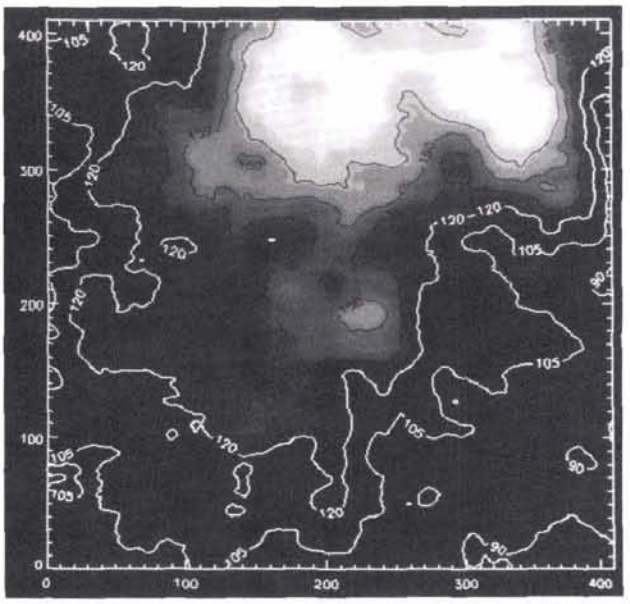

Figure 3. Horizontal variation in the absorption coefficient [a(415)]*1000 for Scene 7. Values have been smoothed by spectrally averaging the three spectral channels centered about 415 nm and applying a 50-by-50-pixel, boxcar average to increase S/N about 85-fold and to reduce contour complexity.

qualitative evaluation of dilution effects on the sediment plume.

The effects of increased CDOM and particle absorption nearshore are visualized for the shorter wavelengths by solving the deep-water, remote-sensing reflectance equation in terms of the absorption coefficient: i.e.,

$$a(\lambda) = b_b(\lambda)[-1 + 0.33/R_{rs}(\lambda)](t/n)^2/Q. \quad (2)$$

For large, whitish, suspended sand particles, the backscattering coefficient is generally nonspectral. Thus, the derived $b_b(671)$ was used in Equation 2 for all wavelengths to derive $a\lambda$) for the shorter wavelengths.

The ebb tidal plume was characterized by the absorption coefficient at 415 nm (see Figure 3). At this short wavelength the absorption coefficient for nearshore waters can be dominated by CDOM (see Carder *et al.*, 1989; 1991), a refractory, rather conservative constituent. The chlorophyll *a* concentration just to the west of this scene at Station 1 was 1.2 mg m^{-3}, so phytoplankton probably contributed less than 0.03 m^{-1} to the absorption coefficient at 415 nm. This is less than one-third of the lowest derived total absorption coefficient shown in Figure 3, and is consistent with the general trend of $a_p = 0.3625\ a_g(415) + 0.0105$ developed in Figure 4 for Stations 1 - 3. Partitioning the absorption coefficient, substituting for $a_p(415)$ in terms of $a_g(415)$, and solving for $a_g(415)$ yields

$$\begin{aligned} a_g(415) &= a(415) - a_w(415) - a_p(415) \\ a_g(415) &= a(415) - a_w(415) - 0.3625a_g(415) - 0.0105 \\ a_g(415) &= (a(415) - 0.0055)/1.3625. \end{aligned} \quad (3)$$

A map of $a_g(415)$ can be derived from the map of $a(415)$, but to convert it into a salinity map, a gelbstoff-salinity relationship is needed. The relationships between $a_g(415)$ and salinity for the 1990 and 1992 data sets are shown in Figure 5a.

The two trends have been fit with linear regression lines with correlation(r^2) coefficients of 0.654 and 0.953, respectively. The 1990 correlation suffered from a paucity of

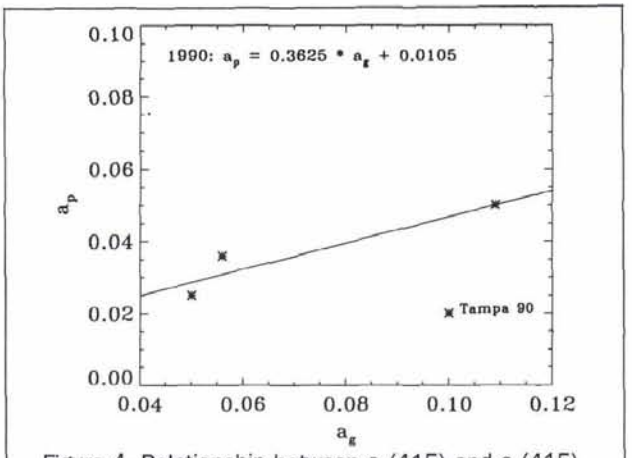

Figure 4. Relationship between $a_p(415)$ and $a_g(415)$ for 4 March 1990.

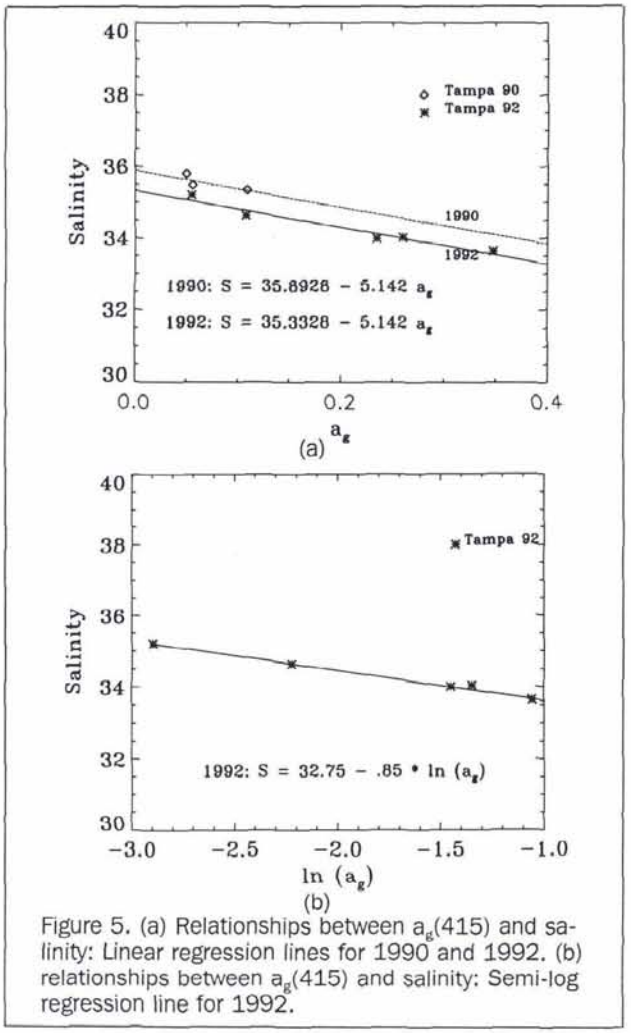

Figure 5. (a) Relationships between $a_g(415)$ and salinity: Linear regression lines for 1990 and 1992. (b) relationships between $a_g(415)$ and salinity: Semi-log regression line for 1992.

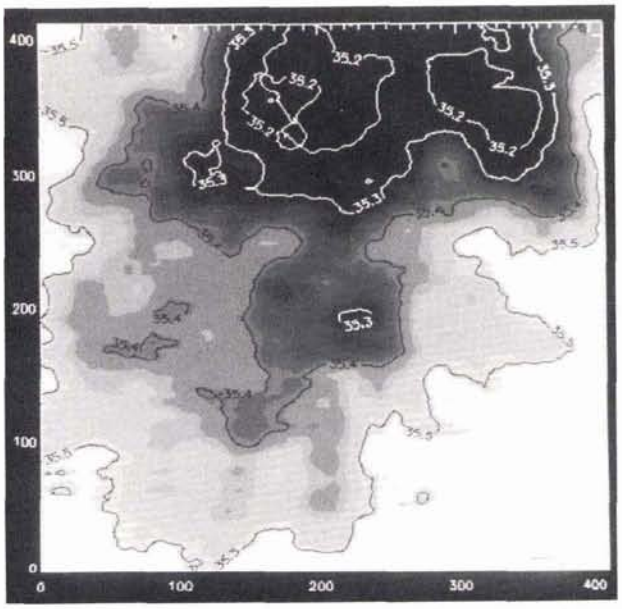

Figure 6. Salinity image map of the mouth of Tampa Bay derived from AVIRIS data.

points, but the curve is generally parallel to and offset from the 1992 curve by about 0.55 g/l. It also was derived with salinity values from conductivity-temperature-depth CTD casts taken at the same station but at slightly different times than the gelbstoff absorption samples. The 1992 subsamples for salinity and gelbstoff absorption measurements were partitioned from the same bottle sample, and thus provided more consistent data.

Discussion

The salinity-gelbstoff absorption data from 1992 are better fit ($r^2 = 0.992$) by the exponential curve, $a_g(415) = \exp[(32.75 - S)/0.85]$ (see Figure 5b) than by a linear one. This relationship suggests a value of 1.0 m^{-1} for $a_g(415)$ at a salinity of 32.75 g/l, reaching a value of zero only for infinite salinity values. It also suggests a value of 5.4×10^{16} m^{-1} for a salinity of 0 g/l, a value perhaps 14 to 15 orders of magnitude higher than found in freshwater sources. This suggests that most of the gelbstoff in Tampa Bay during this low-runoff period was locally produced by phytoplankton nourished by the nutrients brought in by the rivers, rather than being derived solely by river inflow and land runoff.

Because a linear relationship between salinity and $a_g(415)$ indicates a conservative mixing regime between high-salinity, low-gelbstoff outer shelf water and low salinity, high-gelbstoff effluent from the bay, the decreasd rate of reduction in gelbstoff absorption with increasing salinity suggests a locally produced source of gelbstoff in the high-salinity waters. Such exponential curves can be treated as first-order chemical or biological reactions (Lerman *et al.*, 1977). This trend is consistent with those shown in Carder *et al.* (1989) where marine gelbstoff absorption increased with increased primary production.

The fact that a smooth, exponential relationship is encountered suggests that the same waters that are transporting gelbstoff seaward for dilution with shelf waters are also transporting nutrients to maintain the shelf primary productivity and locally generated gelbstoff, with surface salinity values for the eastern Gulf of Mexico rarely exceeding 36.2 g/l. The exponential relationship would suggest a gelbstoff absorption value $a_g(415) = 0.017$ m^{-1} for the outer Florida shelf, a value consistent with measured and modeled data for this region (Carder *et al.*, 1986; 1989). The corresponding linear curve (Figure 5a) produces a negative value of $a_g(415)$ at a salinity value of 36.2 g/l. Clearly this is not possible, so local sources of gelbstoff as waters move offshore and are diluted are required. If shelfbreak upwelling occurs, gelbstoff derived from the increased primary production could produce a_g values at the shelf edge that are higher than ones found immediately shoreward.

In 1990, unfortunately, only one research vessel was involved in the offshore sampling and had to be in relatively clear waters during the AVIRIS overpass in order to recalibrate the sensor (see Carder *et al.*, 1992). As the mission was not as focused upon gelbstoff absorption as in 1992, only a relatively narrow range of salinity and gelbstoff absorption was encountered. Also, the samples were not totally coincident in time and space, resulting in a low correlation coefficient. These limitations were not manifest in the 1992 data set, which produced extremely high correlation coefficients. Had the two field efforts been combined using two ships in 1990, field validation of the images in Figures 2 and 3 could have been undertaken, and a highly correlated, exponential salinity-gelbstoff absorption curve such as shown in Figure 6 could have been used to convert $a_g(415)$ to salinity image maps.

To illustrate the potential such expanded field activities and AVIRIS overflights might provide in the future, the 1990 salinity-gelbstoff curve was used to create a map image of salinity at the mouth of Tampa Bay. We recognize the limitations of this curve, but are convinced from the 1992 data that the actual gelbstoff-salinity relationships for many estuaries, while changing with season due to factors such as runoff, usually give r^2 values of better than 0.95 (e.g., see Berger *et al.* (1984)).

The resulting salinity map image is illustrated in Figure 6, with salinity values ranging from 35.33 to 35.90 g/l. These values are quite high, indicative of the typical dry spring weather found in March. The finesse of the data is rather startling and could be made to be very accurate given a coincident, rapid, salinity-gelbstoff survey down the center of the plume by fast boat(s). This approach would rectify any errors made due to assumptions involved in deriving the $a(415)$ images and provide validation/adjustments for all of the derived data products from AVIRIS.

For waters deeper than 5 or 6 m, the backscattering coefficient at 671 nm varied by a factor of nearly three across Scene 7. Had coincident measurements of suspended particulate matter concentration (SPM), beam transmissometry, or nephelometry been available, $b_b(671)$ images could have been converted to images of SPM, beam attenuation coefficient, or volume scattering function (90°). For such an exercise, multiple ships/boats would be needed, however, due to the rapid temporal and spatial changes expected in suspended sediments in a field of varying wave-current interactions with the bottom. Pollutants coated on suspended particles could likely be mapped using well-validated, AVIRIS-derived backscattering data images. Active resuspension from known bottom pollution sites could be identified at the very least.

The method for deriving $b_b(671)$ can be used for depths as shallow as 1 m if the wavelength is changed to 750 nm. This results from the fact that $a_w(750)$ is 5.74 times as large as $a_w(671$ (Carder *et al.*, 1992). Because of the much smaller $R_{rs}(\lambda)$ values expected at 750 nm, however, significant in-

creases are required in the S/N and the precision needed in removing atmospheric effects from the AVIRIS data.

Conclusions

The use of AVIRIS data to study a coastal environment on the west Florida shelf was accomplished by field-calibrating AVIRIS and removing atmospheric effects from the data using the Lowtran-7 method of Carder *et al.* (1992). The calibrated sensor provided spectral values of water-leaving radiance that were consistent with values measured from a research vessel and with modeled values, provided that the S/N was increased by averaging data.

The absorption coefficient was partitioned into its component parts, and the gelbstoff absorption coefficient a_g was used to derived an image map of salinity. The salinity-gelbstoff relationship determined for the 1990 data set was crude compared to a more focused effort in 1992 when AVIRIS data were unavailable. It was used, however, to illustrate the finesse possible for measuring salinity in the future given a multiple-ship campaign with AVIRIS. Gradations in salinity of 0.05 parts per thousand were readily apparent in the image. For any soluble pollutant covarying with freshwater, derived salinity image maps can be converted to pollutant image maps, providing a rapid and synoptic extrapolation methodology.

Image maps of the backscattering coefficient at 671 nm can likewise be related to the turbidity of the water. Measures of turbidity by nephelometry, for instance, should be directly relatable to the backscattering coefficient because the 90° scatter from particulate matter is closely related to the backscattering coefficient for most aqueous environments (see Kirk, 1983). Any particulate pollutant covarying with turbidity can also be mapped using conversions from $b_b(671)$.

This study shows that coastal applications requiring high-spectral resolution can be accomplished with AVIRIS for non-blue wavelengths, assuming that spatial resolution of better than about 250 m is not required. More recent AVIRIS data sets have reduced levels of coherent noise than our data set contained (e.g., see Hamilton *et al.* (1991)), and planned upgrades to AVIRIS may increase signal levels by 2 to 4 fold at blue wavelengths. Based upon our experience, the increased S/N expected for AVIRIS bodes well for coastal applications requiring an effective spatial resolution of 100 m to 300 m.

Acknowledgments

Special thanks to Thomas Peacock, David Costello, and Lisa Young for their help in field sampling and with laboratory analyses. Financial support was provided by the National Aeronautics and Space Administration to the University of South Florida (USF) through grant NAGW-465, GSFC contract NAS5-30779, and JPL contract 958914 (RE-198), and by the Office of Naval Research through grant N00014-89-J-1091 to USF. Ship support was provided by the State of Florida through the Florida Institute of Oceanography.

References

Berger, P., R. W. P. M. Laane, A. G. Ilahude, M. Ewald, and P. Courtot, 1984. Comparative Study of Dissolved Fluorescent Matter in West-European Estuaries, *Oceanol. Acta* 7:309–314.

Bricaud, A., A. Morel, L. Prieur, 1981. Absorption by Dissolved Organic Matter in the Sea (Yellow Substance) in the UV and Visible Domains, *Limnol. Oceanogr.*, 26:43–53.

Carder, K. L., and R. G. Steward, 1985. A Remote-sensing Reflectance Model of a Red Tide Dinoflagellate Off West Florida, *Limnol. Oceanogr.*, 30:286–298.

Carder, K. L., and R. G. Steward, J. H. Paul, and G. A. Vargo, 1986. Relationships Between Chlorophyll and Ocean Color Constituents as They Affect Remote-Sensing Reflectance Models, *Limnol. Oceanogr.* 31:403–413.

Carder, K. L., R. G. Steward, G. R. Harvey, and P. B. Ortner, 1989. Marine Humic and Fulvic Acids: Their Effects on Remote Sensing of Ocean Chlorophyll, *Limnol. Oceanogr.*, 34:68–81.

Carder, K. L., S. K. Hawes, K. A. Baker, R. C. Smith, R. G. Steward, and B. G. Mitchell, 1991. Reflectance Model for Quantifying Chlorophyll a in the Presence of Productivity Degradation Products, *J. Geophys. Res.*, 96(C11):20599–20611.

Carder, K. L., P. Reinersman, R. F. Chen, F. Muller-Karger, C. O. Davis, and M. Hamilton, 1992. AVIRIS Calibration and Application in Coastal Oceanic Environments, *Remote Sensing of Environment*, Special Issue on Imaging Spectrometry (G. Vane, editor), submitted.

Gordon, H. R., 1979. Diffuse Reflectance of the Ocean: The Theory of Its Augmentation by Chlorophyll a Fluorescence at 685 nm, *Appl. Opt.*, 18(8):1161–1166.

Gordon, H. R., and A. Morel, 1983. *Remote Assessment of Ocean Color for Interpretation of Satellite Visible Imagery: A Review*, Springer.

Gregg, W. W., and K. L. Carder, 1990. A simple 1 nm Resolution Solar Irradiance Model for Cloudless Maritime Atmospheres, *Limnol. Oceanogr.*, 35:1657–1675.

Hamilton, M., C. O. Davis, S. H. Pilorz, W. J. Rhea, and K. L. Carder, 1991. Examination of Chlorophyll Distribution in Lake Tahoe, Using the Airborne Visible and Infrared Imaging Spectrometer (AVIRIS), *Proceeding of the Third AVIRIS Workshop*, JPL Pub. No. 91–28.

Holm-Hansen, O., and E. Riemann, 1978. Chlorophyll-a Determinations: Improvement in methodology, *Oikos* 30:438–447.

Lerman, A., K. L. Carder, and P. R. Betzer, 1977. Elimination of Fine Suspensoids in the Oceanic Water Column, *Earth Planet Sci. Let.*, 37:61–70.

Marshall, B. R., and R. C. Smith, 1990. Raman Scattering and In-water Ocean Optical Properties, *Appl. Opt.*, 29:71–84.

Mitchell, B. G., 1990. Algorithms for Determining the Absorption Coefficients for Aquatic Particulates Using the Quantitative Filter Technique, *Ocean Optics X, Proc. SPIE*, 1302:137–148.

Morel, A., and L. Prieur, 1977. Analysis of Variations in Ocean Color, *Limnol. Oceanogr.*, 22:709–722.

Muller-Karger, F. E., C. R. McClain, and P. L. Richardson, 1988. The Dispersal of the Amazon's Water, *Nature*, 333:56–59.

Muller-Karger, F. E., C. R. McClain, T. R. Fisher, W. E. Esaias, and R. Varela, 1989. Pigment Distribution in the Caribbean Sea, *Prog. Oceanog.*, 23:23–64.

Peacock, T. G., K. L. Carder, C. O. Davis, R. G. Steward, 1990. Effects of Fluorescence and Water Raman Scattering on Models of Remote Sensing Reflectance, *Ocean Optics X, Proc. SPIE*, 1302:303–319.

Smith, R. C., and K. S. Baker, 1984. The Analysis of Ocean Optical Data, *Ocean Optics VII, Proc. SPIE*, 489:119–126.

———, 1986. The Analysis of Ocean Optical Data, 2, *Ocean Optics VIII, Proc. SPIE*, 637:95–107.

Stavn, R. H., 1990. Raman Scattering Effects at the Shorter Visible Wavelengths in Clear Ocean Waters, *Ocean Optics X, Proc. SPIE*, 1302:94–100.